J Nanostruct 16(2): 1760-1780, Spring 2026

RESEARCH PAPER

Novel Nano Schiff Base Ligand and its Metal Complexes: Synthesis, Structural Investigation, Molecular Docking, Antibacterial Screening and Anticancer Evaluation Against PC-3 Cells

Nesser Kadham Shareef [1], *Fawzi Yahya Wadday* [2*]

[1] *Department of Chemistry, Faculty of Science, Karbala University, Kerbala, Iraq*

[2] *Department of Chemistry, Faculty of Science, Kufa University, Al-Najaf, Iraq*

ARTICLE INFO

Article History:
Received 23 December 2025
Accepted 26 March 2026
Published 01 April 2026

Keywords:
Azomethine
Cancer cells
Complexes
Nano Schiff Base
Pathogenic bacteria

ABSTRACT

A novel nano ligand, N- (4-chloro-2-(((Z)-4-methoxybenzylidene) amino)-5-methylphenyl)-1-(4-methoxyphenyl) methanimine (MAPM), was created by the reaction(1mol) of 4-chloro-5-methylbenzene-1,2-diamine with (2 mol) 4-methoxybenzaldehyde in anhydrous ethanol. The nano mononuclear complexes of this ligand was created with Ni(II), Cu(II), Pt(IV), Pd(II), Ag(I), and Au(III) ions. The compounds were recognized by means of mass spectrometry, ^{1}HNMR and ^{13}C NMR spectroscopy, elemental analysis (C, H, N), atomic absorption, UV-Vis and (FT-IR), magnetic susceptibility and molar conductivity as well as XRD and FE-SEM, revealed the nanoscale properties of the compounds. The measured data regarding the composition of the metal complexes and the elemental analysis confirmed that the ratio of metal to ligand is of the type [M(L)], where M is Pd(II), Ag(I), Au(III) and [M(L)2], where M is Ni(II), Cu(II), Pt(IV) and (MAPM) is a azomethine ligand. Previous measurements from tetrahedral geometry for Ag(I) complexes, square planar for Au(III) and Pd(II)complexes while the other complexes are an octahedral geometry for Ni(II),Cu(II)and Pt(IV)ions are discussed. All complexes exhibited non-electrolytic characteristics, except for the silver and gold complexes, which were conductive. The compounds also demonstrated a high degree of temporal stability and effective inhibitory activity towards two bacteria that are pathogenic, S. aureus and E. coli. The investigation also included the in vitro assessment of the toxicity of MAPM and its Pd(II) complex towards human prostate cancer cells (PC-3) and other cells that are normal. Compared to the ligand, the Pd(II) complex has a higher affinity for cancer cells, it has no effect on non- cancer cells.

How to cite this article
Kadham Shareef N., Yahya Wadday F. Novel Nano Schiff Base Ligand and its Metal Complexes: Synthesis, Structural Investigation, Molecular Docking, Antibacterial Screening and Anticancer Evaluation Against PC-3 Cells. J Nanostruct, 2026; 16(2):1760-1780. DOI: 10.22052/JNS.2026.02.028

INTRODUCTION

Both the industrialized and developing worlds are at risk from microbial illnesses, which have plagued human civilization since prehistoric times and account for a significant percentage of fatalities globally, and cancer, a terrible and deadly illness for which there is no suitable treatment [1]. In coordination and biological chemistry, Schiff bases are a significant family of organic molecules that have drawn a lot of interest [2].

* *Corresponding Author Email: fawzi.almwuashi@uokufa.edu.iq*

Since the azomethine nitrogen atom has a high electron density, Schiff bases are among the most potent chelators. Since it has been shown that chelating Schiff bases with transition metal ions enhances their biological potential, metal complexes of different Schiff bases are well-known for their anti-inflammatory, anti-bacterial, anti-fungal, anti-cancer, and antitubercular properties [3, 4]. Ongoing research endeavors worldwide are focused on investigating safe and efficient biologically active molecules based on metals as possible antibacterial medications [5]. Out of all the treatment strategies to eradicate these microbiological threats, the evaluation of transition metal complexes as metallo-drugs has shown their considerable promise [3]. Inhibition of enzymes, contact with intracellular biomolecules, increased lipophilicity, modification of cell membrane activities, cell cycle arrest, etc. are some of the ways that metal complexes are thought to work [6]. Metal complexes are expected to change their kinetic and thermodynamic characteristics toward biological receptors because of a broad range of coordination spheres, ligand designs, oxidation states, and redox potentials [7]. Chelation therefore results in significant alterations to the biological characteristics of both the metal moiety and ligands [8]. Here, metal complexes with exceptional biological activity such as antifungal, anticancer, and antibacterial properties, are formed from Schiff bases, which are produced when condensed aromatic diamines and methoxy benzaldehyde combine. An analysis was conducted on the newly created complexes of nickel (II), palladium (II), platinum (IV), copper (II), silver, and gold (III). Additionally, the antibacterial activity was assessed against strains of Staphylococcus aureus and Escherichia coli using the paper disc diffusion technique (for qualitative assessment) and the serial dilutions in liquid broth method (for determination of minimum inhibitory concentration). The palladium (II) complex and (MAPM) were tested for their antiproliferative properties against PC-3 prostate cancer cell lines. The method of action of these drugs was finally clarified by molecular docking research, which supports the efficient binding of molecules to the protein's active region.

MATERIALS AND METHODS

Instrumentation

Bruker D.R.X. (DMSO-d6, 125 MHz, 500 MHz) Stuart provided the ^{13}C, ^{1}H nuclear magnetic resonance spectrometer, 5975 quadrupole mass spectrometer, Euro Vectro-3000A trace element analyzer, Jena atomic absorption spectrometer (VARIO 6, AG), Shimadzu's UV-visible spectrophotometer 1700 (wavelength 200-1100 nm), Shimadzu's Fourier transform infrared spectrometer (wavelength 440-4000 cm^{-1}). Scanning electron microscopy (FE-SEM) images of the compounds were taken using a Zeiss EM3200 microscope. X-ray diffraction (XRD) was recorded using a Philips diffractometer with a graphite crucible as its only component. The device employed Cu kα type radiation (wavelength = 1.54 Å) as the X-ray source at 45 kV and 50 mA. The quantity of chloride in Ni(II), Cu(II), Pd(II), Pt(IV), and Au(III) complexes was measured using $AgNO_3$ solutions. To determine the whole composition of the substances, thin layer chromatography(TLC) was employed. A few selected samples were subjected to activity assessments at the Al-Ameen Center for Advanced Research and Biotechnology. The Beckman Model J2-21 chilled centrifuge and the Marubeni freezer (-800 degrees Celsius) were manufactured in the United States. Machine for distillation the drying and sterilizing apparatus was built by Hermle, Germany, and Ogawa Seiki. Organon Teknika was constructed incubators and readers. Germany's Leica inverted microscope. Microplates, multiwell plates, and 96-well plates were manufactured in the United States (USA). Microporous membranes that can pass through a filter with a porosity of 0.22 µm. Sterilized vials for tissue culturing (25.75 cm^2). Water bath and water pump.

Materials

4-methoxybenzaldehyde, 4-chloro-5-methylbenzene-1,2-diamine, metal chlorides ($NiCl_2.6H_2O$, $CuCl_2.2H_2O$,$PdCl_2$ and $H[PtCl_6].6H_2O$, $H[AuCl_4]$, $AgNO_3$, as well as Müller-Hinton agar, absolute ethanol, glacial acetic acid, acetone, acetonitrile, diethyl ether, dimethylsulfoxide (DMSO), hexane, N,N-Dimethylformamide (DMF), ethyl acetate. All chemicals and solvents were of the highest quality and were sourced from Sigma-Aldrich. BDH and Fluka were employed without additional manipulation.

Synthesis of New ligand (MAPM)

The synthesis of the ligand, N- (4-chloro-2-(((Z)-4-methoxybenzylidene)amino)-5-methylphenyl)-

1-(4-methoxyphenyl) methanimine (MAPM):

(1.17 gm, 0.0086 mol) of 4-methoxybenzaldehyde and (0.67 gm, 0.0043 mol) of 4-chloro-5-methylbenzene-1,2-diamine dissolved in 20 ml of hot absolute ethanol were reacted to produce the L_1(MAPM) molecule, which was then acidified by three drops of glacial acetic acid [9]. The reaction mixture was refluxed at 75°C with continuous and powerful magnetic stirring to ensure the homogeneity of the mixture and control over the nucleation process; this temperature was maintained for approximately 240 minutes to allow for controlled thermal homogeneity. After the reaction was complete, heating was stopped, and the mixture was allowed to cool naturally to room temperature. The resulting suspension was then left undisturbed for 8 hours to promote controlled crystallization and prevent agglomeration. The reaction's progress was tracked using TLC by employing hexane–ethanol (4:6) (v/v) as the eluent and the formation of a reddish-brown crystalline substance. After that, cold dry ether was used to filter and wash the chemical [10]. Following oven drying, the solid's yield was 87%. Fig. 1 illustrates the (MAPM) creation reaction.

Preparation of Pd(II) as $Pd(CH_3CN)_2Cl_2$

A solution of 1.0 g $PdCl_2$ in 20 ml acetonitrile is prepared. The combination underwent a one-hour reflux. Following the addition of 50 milliliters of diethyl ether, a pale orange precipitate of $Pd(CH_3CN)_2Cl_2$ is produced. The precipitate was filtered and washed with diethyl ether [10].

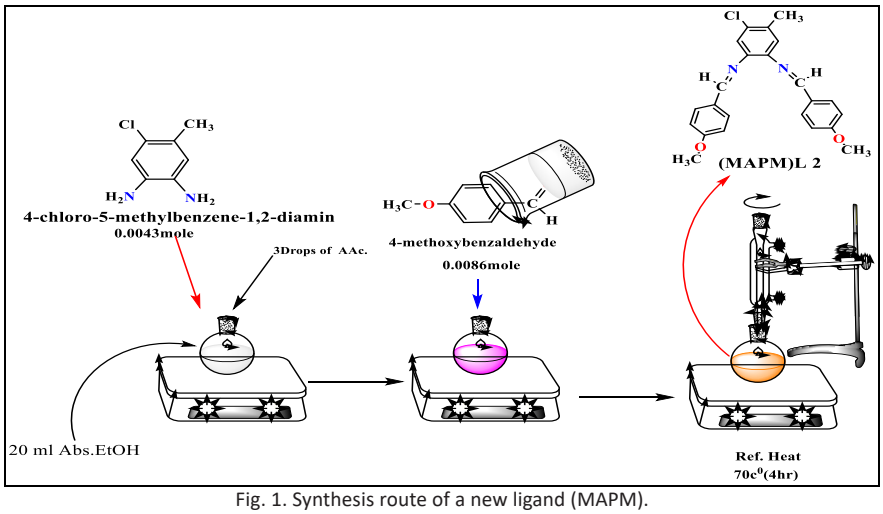

Fig. 1. Synthesis route of a new ligand (MAPM).

Table 1. Specific physical and chemical characteristics of the Schiff base ligand (MAPM) and its complexes.

Chemical formula	Color	M.Wt g/Mole	M.P°C	Yield%	Mole ratio M:L
(MAPM), L_1= $C_{23}H_{21}ClN_2O_2$	Reddish brown	392.883	155-157	87	/
$[Ni(MAPM)_2\ Cl_2]H_2O$	Light brown	933.37	178-180	80	1:2
$[Cu(MAPM)_2\ Cl_2]H_2O$	Light green	920.212	173-175	84	1:2
$[Pt(MAPM)_2\ Cl_2]Cl_2.H_2O$	Pale yellow	1140.6	201-203	80	1:2
[Pd (MAPM) Cl_2]	Yellowish brown	570.2	188-189	85	1:1
$[Ag(MAPM)\ (H_2O)_2]NO_3$	Light brawn	598.785	163-164	71	1:1
[Au(MAPM) Cl_2]Cl	Light yellow	696.2	170-172	78	1:1

Preparation of Metal Salts Standard Solutions

To make the metal salts standard solutions, the required weight (0.0001 mol) of each of the following salts was dissolved to create a stock solution with a concentration of $1x10^{-3}$ M $NiCl_2.6H_2O$, $CuCl_2.2H_2O$, $H_2[PtCl_6].6H_2O$, $Pd(CH_3CN)_2Cl_2$, $AgNO_3$ and $H[AuCl_4]$ in 100 milliliters of absolute ethanol solvent. The standard solutions mentioned above were used to create a number of concentrations that ranged from 1×10^{-4} to 1×10^{-6} M [11].

Mole Ratio Method

The absorption spectra of a variety of mixed solutions were measured, including one milliliter of the metal ion salt at the optimal concentration and varying volumes of the ligand solution at the same concentration. The relationship between the absorbance on the Y-axis and the mole ratio on the X-axis was plotted to get the (M:L) ratio. The M:L ratio is represented by the intercept of the two lines of straight ion complexes, and it was 1:1 except for the Ni(II),Cu(II) and Pt(IV) complexes they were 1:2 (M:L) ratio with the MAPM ligand [12].

Synthesis of ligand(MAPM)-Metal complexes

With the exception of Ni-L, Cu-L and Pt-L which had mole ratios of M:L (1:2), the other complexes were synthesized in a mole ratio of M:L (1:1) for Pd, Ag and Au ions. A little quantity of heated absolute ethanol was used to dissolve the (MAPM) ligand (0.784 g, 2 mmol) Scheme (2). The proper absolute ethanol solution of metal salts was progressively supplemented with the ligand solution [13]. The reaction mixture was heated to reflux for (90-120 minutes) and under similar working conditions in the preparation of the ligand, after the addition of $NiCl_2.6H_2O$ (0.236gm,1 mmol),

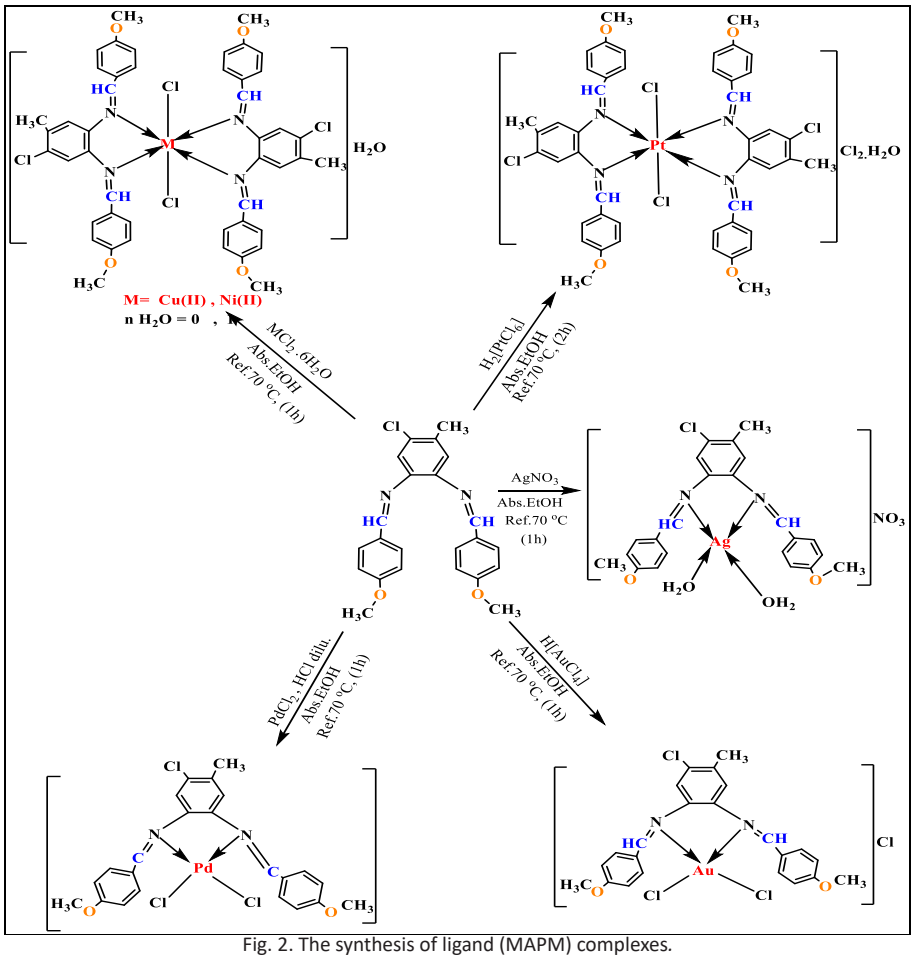

Fig. 2. The synthesis of ligand (MAPM) complexes.

$CuCl_2.2H_2O$ (0.17gm, 1 mmol), $H_2[PtCl_6].6H_2O$ (0.516gm,1 mmol), while (0.392 gm,1mmol) from (L) equivalent amount to $Pd(CH_3CN)_2Cl_2$ (0.259 g,1 mmol), $AgNO_3$ (0.1698 g, 1 mmol), and $H[AuCl_4]$ (0.339,1 mmol). After being washed with diethyl ether, the solid crude material was filtered and oven-dried, then each compound was dissolved in absolute ethanol and ultrasonically treated at a frequency of 20–40 kHz for 20 minutes while maintaining a temperature below 40 °C, with the aim of reducing agglomeration and improving nanodispersion without affecting the coordination structure. The compounds were then separated, washed, and dried [14]. The different quantities of ligand as well as the per cent composition of all forming complexes are shown below in the Table 1 and Fig. 2.

Antimicrobial Study

All of the recently developed ligand and complexes were assessed for their antibacterial abilities against *Staphylococcus aureus* (a bacterium that is gram-positive), as well as against *E. coli* (a bacterium that is gram-negative), using the agar diffusion method [14]. All compounds showed a capacity to combat bacteria. Mueller-Hinton broth was used as the medium for the growth of the test organisms. Dimethyl sulfoxide (DMSO) at a concentration of $1x10^{-3}$ M was used as the solvent for chemical solutions that are intended for biological research [15]. The plates were placed in a warm incubator at 37°C for a day. The efficacy of the compounds synthesized in this manner as antibacterial was determined by the size of the inhibitory zone formed by the compounds against the respective test bacterium. The volume of the area of growth restriction for each sample was calculated using the average of three separate replicates in order to have a conclusion [16].

Cell cytotoxicity (In Vitro Cytotoxicity) and viability tests

Cell line

The PC-3, purchased from the Pastor Institute in Iran, was utilized in this investigation, and cancer cells were grown and tested at the University of Tehran.

Development of a prostate cancer cell line(PC-3)

PC-3 cells were cultivated using the Freshney method as described below. Prostate cancer cells (PC-3) were properly thawed and then placed in a 37°C water reservoir. A culture of 25 cm^2 cells containing culture medium (RBMI-1640) and (10%) bovine serum was maintained at 37°C, 5% CO_2 for 24 hours. After 24 hours, the cells were observed under a microscope to assess their viability, lack of contamination, and the number of cells that had been cultured (approximately 500,000-800,000 cells/ ml). The cells were then moved to a chamber that had a growth purpose, the spent medium from the culture was discarded, and the cells were washed with PBS (a physiological solution that stains cells) [16]. The cells were then treated with the appropriate amount of trypsin and incubated at 37°C for 30-60 seconds. The cells were inspected frequently until the monolayer of cells was converted into a single cell type. New culture medium that was free of calf serum was then incorporated into the mix to halt the addition of enzymes. Carefully separate the cells by taking a 10-minute spin at 2000 RPMs in a room temperature to collect the cells. Throw away the wasted medium and trypsin, gently reattached the cells to the new medium, this medium had 10% fetal calf serum as its sole component. figure out how many cells are in the cell suspension by adding the same volume of the cell suspension to the same amount of Trepana Blue dye [17]. Use a hemocytometer to count the cells and assess their viability, the formula for this is as follows:

$$C = N \times 10^4 \times F/Ml$$

C is the number of cells in 1 ml of the solution, N is the number of cells on the slide, F is the ratio of cells to be studied, and 10 is the size of the slice. The cell survival rate of the sample was determined with a hemocytometer chip.

Viability ratio = (the number of living cells/the number of deceased cells) times 100%.

The cell solution was then transferred to a new container and incubated at 37°C, 5% CO_2 for 24 hours.

The MTT staining test for the viability of prostate cancer cells (PC-3)

Cell growth and cell viability were quantified using the MTT [3-(4, 5-dimethylthiazol-2-yl)-2, 5-diphenyltetrazolium Bromide] (Sigma-Aldrich) assay. In brief, for monolayer culture, cells were digested with trypsin, harvested, adjusted to a density of 1.4×10^4 cells/well and seeded to 96-

well plates filled with 200 µl fresh medium per well for 24 h. When cells formed a monolayer, they were treated with 300-3.7 µg/ml of the ligand(MAPM) and its Pd(II)-complex for 24 h at 37 °C in 5% CO_2. At the end of the treatment (24 h), while the monolayer culture was left untouched in the original plate, the supernatant was removed and 200 µl/well of MTT solution (0.5 mg/ml) in phosphate-buffered saline [PBS]) was added and the plate was incubated at 37 °C for an additional 4 h [18]. MTT solution (the supernatant of cells was removed and dimethyl sulfoxide was added 100 µl per well). Cells were incubated on a shaker at 37 °C until crystals were completely dissolved. Cell viability were quantified by measuring absorbance at 570 nm using an ELISA reader (Model wave xs2, BioTek, USA). The concentration of the compounds that resulted in 50% of cell death (IC_{50}) was determined from respective dose-response curves.

RESULTS AND DISCUSSION

The analysis of the ligand (MAPM) and its associated metal ions is described in detail.

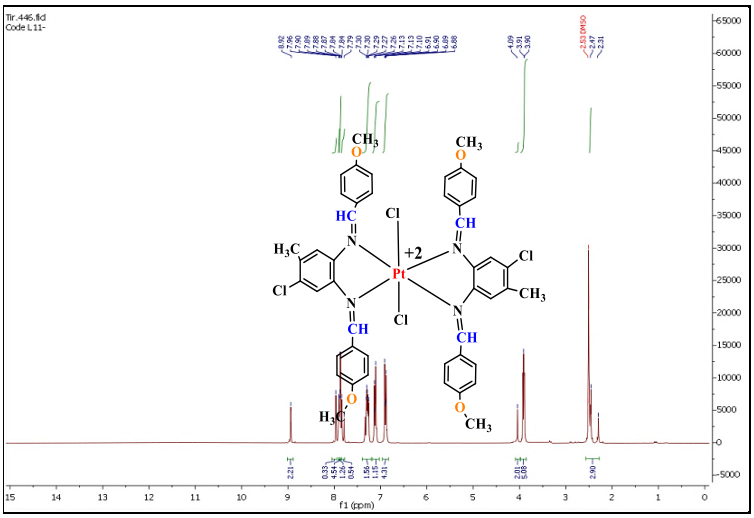

Fig. 3.^{1}HNMR Spectrum of $[Pt(MAPM)_2Cl_2]Cl_2.H_2O$ complex.

Table 2. Analysis of the elemental composition of the ligand (MAPM) and its metal complexes.

Chemical formula	Element analysis found (calc.)%				
	M.wt	C	H	N	M
L_1(MAPM)= $C_{23}H_{21}ClN_2O_2$	392.88	th.70.31 ex.(70.38)	5.39 5.46)(	7.13 7.31)(	/
$[Ni(C_{46}H_{42}Cl_4N_4O_4)]H_2O$	933.37	59.19 (59.38)	4.75 (4.98)	6.00 (5.88)	6.29 6.07)(
$[Cu(C_{46}H_{42}Cl_4N_4O_4)]H_2O$	920.212	60.04 (60.15)	4.60 (4.49	6.09 (6.26)	6.91 (7.23)
$[Pt(C_{46}H_{42}Cl_4N_4O_4)]Cl_2.H_2O$	1140.6	48.44 (48.32)	3.89 (4.11)	4.25 (4.32)	17.1 (16.83)
Pd ($C_{23}H_{21}Cl_3N_2O_2$)]	570.2	48.45 48.52)(	3.71 (4.01)	4.91 (5.11)	18.66 (17.84)
$Ag(C_{23}H_{25}ClN_2O_4)]NO_3$	598.785	46.14 (46.21)	4.21 4.18)(	7.02 (7.17)	18.01 (17.81)
$Au(C_{23}H_{21}Cl_3N_2O_2)]Cl$	696.2	39.68 (39.77)	3.04 (3.21)	4.02 (4.32)	28.29 (27.93)

Physical characteristics and elemental examination

The ligand used in this study (MAPM) is reddish brown in color. This ligand redeems the used metal ions to give a compound different colours in their crystallization process. Regarding the reaction with air, none of the compounds are affected since they are not soluble in water. However, they are soluble in polar organic solvents such as methanol, ethanol, diethyl ether, acetone, carbon tetrachloride and dimethyl sulfoxide. Physical characteristics and the elemental analysis (C.H.N) analyses of the compound are presented in Table 2 besides the metallic constituents in the organized compounds. The obtained investigative data is sufficient for the investigated values of the intended magnitudes, where the complexes analytical data are well matched with the obtained experimental results data. The value shows 1:2 ratio of the metal to ligand at Ni(II), Cu(II) and Pt(IV), which was consistent with octahedral geometry. At the same time, the Ag(I) with tetrahedral while the Pd(II) and Au(III) complexes were square planar, at 1:1 ratio of the metal to the ligand.

N.M.R Spectra for the (MAPM) ligand and Pt-complex

The NMR spectral data for (MAPM) and its complex have been recorded in DMSO-d^6 solution. For the spectrum of (MAPM)showed a signal at 8.88 ppm ascribed to the azomethine proton (-CH=N), which shows that the Schiff base ligand has been formed. The aromatic ring protons resonate between 6.84 and 7.75 ppm, while for the singlet at 3.84 ppm was found in the methoxy–OCH_3 protons. Additionally, the peak at 2.42ppm attributed to the methyl protons [16].

The proton spectrum of the diamagnetic Pt-MAPM complex were a singlet from the azomethine proton (-N=CH-) was visible at 8.92 ppm. The aromatic ring protons were seemed at (δ=7.30-6.89) ppm and (7.96-7.79) ppm due to benzaldehyde and phenyl diamine rings protons. In addition to the signal at (δ=4.09 ppm) assigned to methoxy protons that attached directly to the benzaldehyde ring in Pt^{4+} complex [19], and the singlet signals at (δ=2.31 ppm) assigned to methyl protons that attached directly to the benzene diamine ring. This peaks for Pt-MAPM complex has changed to in the downfield, which may be due to lone pair electrons contributing to the central metal ion and formation of the nitrogen- Pt^{+4} linkage [19]. The chemical shifts are displayed in Fig. 3.

The ^{13}C NMR spectra of the compound (MAPM) in DMSO-d_6 exhibit a signal 160.97 for C6=N were assigned to the azomethine carbon atoms. The signal at 165.08,129.79ppm was designated for C3,C4 in benzaldehyde ring. The shift at δ(56.18 ppm) assigned to the (C5)carbons methoxy (CH_3-O) [20]. The chemical shift at δ(142.38ppm) is due to (C8–N)and (C7-N), while the chemical shifts appeared at δ(130.98,116.23 ppm) attributed to (C1,C2) in benzaldehyde ring, also shifts appeared at δ(127.84 ppm) and (123.00 ppm) assigned

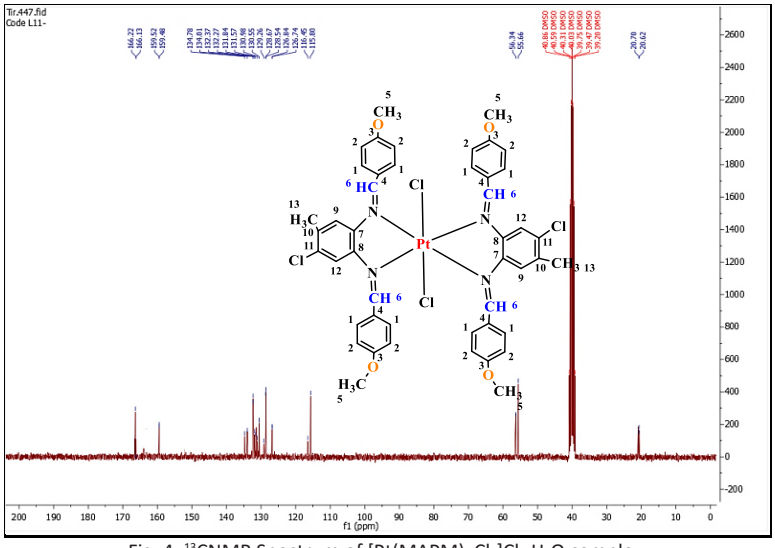

Fig. 4. ^{13}CNMR Spectrum of $[Pt(MAPM)_2Cl_2]Cl_2.H_2O$ complex.

to (C9,C12) in the benzene diamine rings, while the chemical shifts appeared at δ(135.59) and δ (135.55) ppm attributed to C10, C11 atoms. The aliphatic methyl groups carbon atoms (C13),associated with benzene diamine ring at 20.69 ppm [21].

A ^{13}C-NMR spectrum of Pt^{+4} complex Fig. 4, appeared slight difference in chemical shifts from the ligand spectrum. A chemical shift, at δ(166.22 ppm) assigned to the atom (C6=N) of azomethine [22]. The shift at δ(166.13ppm) assigned to the (CH_3O-C3) in benzaldehyde rings atoms. The

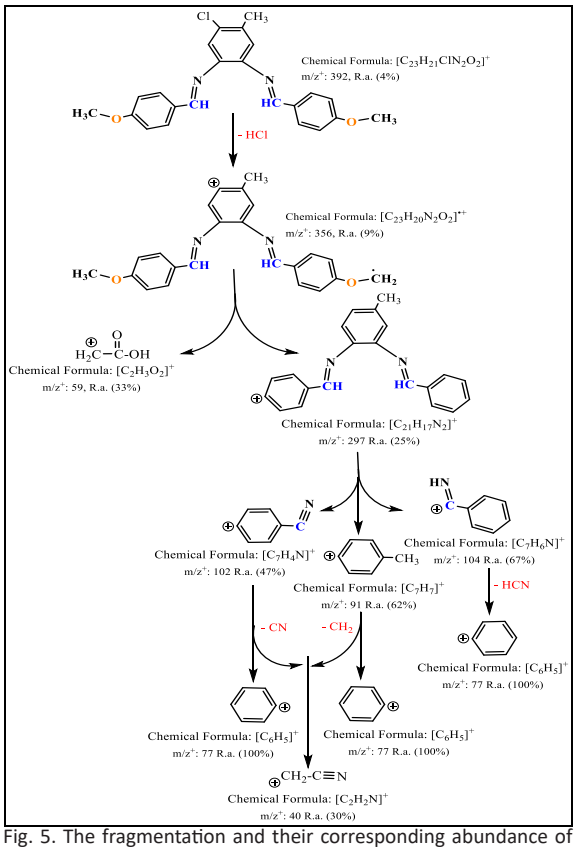

Fig. 5. The fragmentation and their corresponding abundance of MAPM.

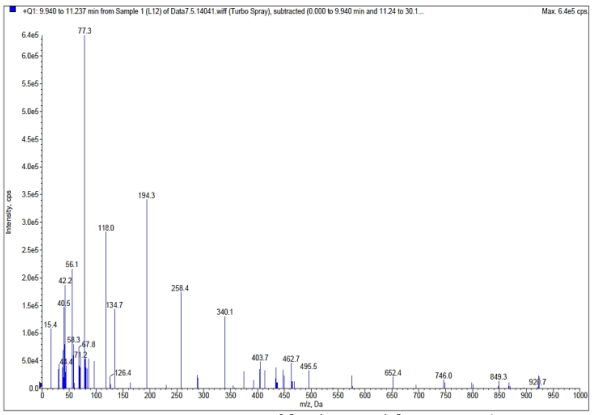

Fig. 6. Mass spectrum of $[Cu(MAPM)_2]H_2O$ complex.

chemical shift at δ(134.78,134.01 ppm) is due to (C8,C7), while the chemical shifts appeared at δ(132.37, 132.27 ppm) attributed to (C10,C11), also shifts appeared at δ (126.84,126.74ppm) assigned to and (C9,C12) in the benzene diamine rings, while the chemical shifts appeared at δ(130.55,115.8) ppm and (126.84ppm) attributed to C1, C2 and C4 atoms in benzaldehyde ring. The aliphatic methyl groups carbon atoms (C5, C13) appeared at δ(55.66, 20.62 ppm) [23].

Mass Spectrum of (MAPM) ligand and its $[Cu(MAPM)_2Cl_2]H_2O$ complex

To compare their stoichiometric composition,

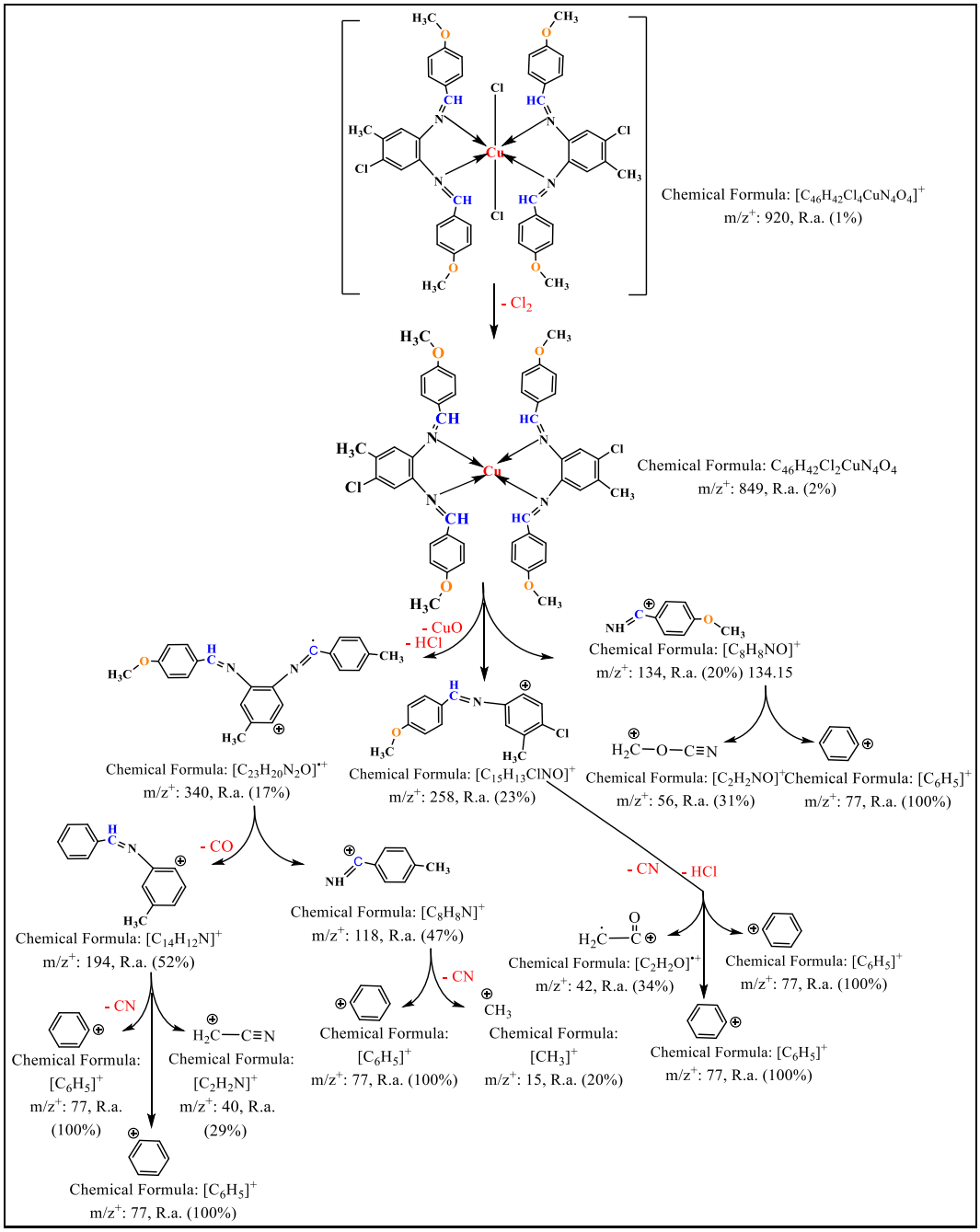

Fig. 7. The fragmentation and their relative abundance of $[Cu(MAPM)_2]H_2O$ complex.

the mass spectrum of the (MAPM) and its metal complex were acquired. As a parent ion peak associated to (M+), the base peak at (m/z^+=392.8) in the mass spectrum of (MAPM),, is thought to be a good indication of the newly created ligand Fig. 5 display the remaining pieces together with their relative abundances and fragmentation paths. The [M·+] peaks at m/z^+ 920 were also generated by the $[Cu(MAPM)_2]H_2O$, Fig. 6, which is in agreement with the suggested chemical formula. All of these mass spectrum peak values for (MAPM) and its studied metal complex support the anticipated chemical formula of the compounds [24]. The leftover pieces, their relative abundances, and the fragmentation routes for the Cu-complex are shown in Fig. 7.

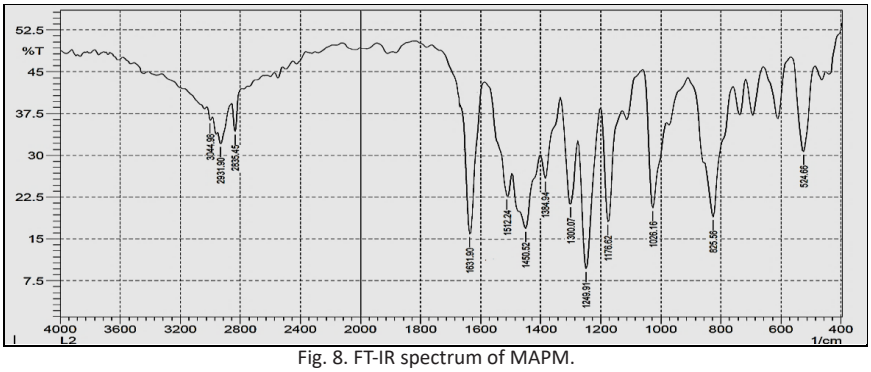

Fig. 8. FT-IR spectrum of MAPM.

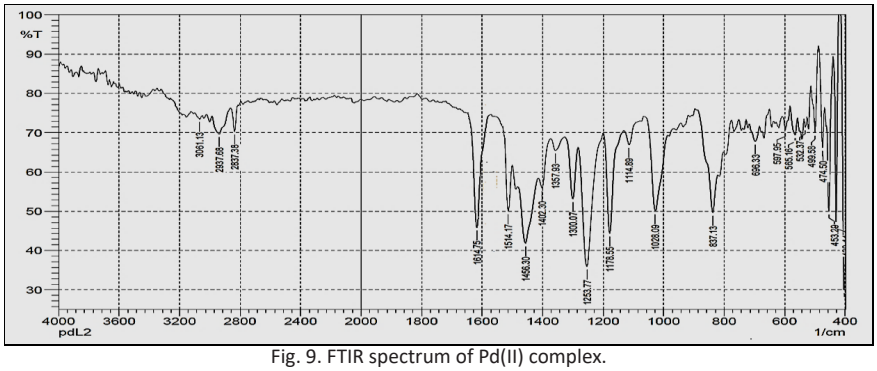

Fig. 9. FTIR spectrum of Pd(II) complex.

Table3. IR spectra of the (MAPM) and its complexes (υ in cm^{-1})

Chemical formula	υ (C=N)	υ (O-H) Hydrate	H_2O δ Bending	υ (M-N)	υ (M-O)
$(MAPM)L_1=C_{23}H_{21}ClN_2O_2$	1631	/	/	/	/
$[Ni(C_{46}H_{42}Cl_4N_4O_4)]H_2O$	1617	3419	835	617-467	/
$[Cu(C_{46}H_{42}Cl_4N_4O_4)].H_2O$	1616	3428	839	536-497	/
$[Pt(C_{46}H_{42}Cl_4N_4O_4)]Cl_2.H_2O$	1611	3564	/	518-474	/
$[Pd(C_{23}H_{21}Cl_3N_2O_2)]$	1614	/	/	532-499	/
$[Ag(C_{23}H_{25}ClN_2O_4]NO_3$	1615	3440	831	540-468	456
$[Au(C_{23}H_{21}Cl_3N_2O_2)]Cl$	1615	/	/	534-471	/

FTIR Spectra of Ligand (MAPM) and its metal Complexes

The IR spectral data obtained for the Schiff base ligand (MAPM) has been taken and contrasted with those of its complexes in order to elucidate on the' possible coordinating sites in the formation of complexes as found in Figs. 8 and 9. The obtained data is listed in Table 3 with some of the most important assignment of the characteristic bands. The spectrum of the ligand, Fig. 8 shows the

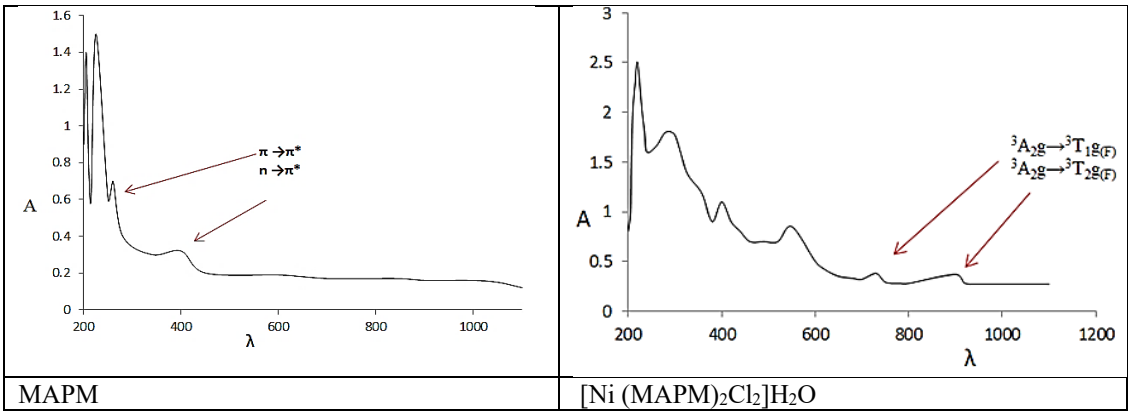

Fig. 10: Electronic spectrum of Pd(II) complex with MAPM.

Table 4. Electronic spectra, magnetic measurements, geometries and hybridization of metal complexes of ligand (MAPM) under study at laboratory temperature.

Compounds	λ_{max} (nm)	Abs. bands (cm^{-1})	Transitions	μ_{eff} (B.M)	Geometry	Hybrid.
L_1	400	25000	n →π*	-	-	-
	260	38461	π →π*			
	225	4444				
Ni(II)-Complex	800	12500	$^3A_2g \rightarrow {}^3T_2g_{(F)}$	2.988	Octahedral	sp^3d^2 High spin
	615	16260	$^3A_2g \rightarrow {}^3T_1g_{(F)}$			
	520	19230	$^3A_2g \rightarrow {}^3T_1g_{(P)}$			
	410	24390	n →π*			
	290	34482	π →π*			
Cu(II)-Complex	670-760	14925-13157	$^2E_2g \rightarrow {}^2T_2g$	1.87	Octahedral (Distorted) (Z-out)	sp^3d^2 High spin
	450	22222	n →π*			
	300	33333	π →π*			
	210	47619	π →π*			
Pt(II)-complex	620	15625	$^1A_1g \rightarrow {}^1T_1g_{(F)}$	Diamagnetic	Octahedral	d^2sp3
	560	17857	$^1A_1g \rightarrow {}^1T_2g_{(F)}$			
	385	25974	π →π*			
	320	31250	π →π*			
	460	21739	n →π*			
Pd(II)-Complex	640	15625	$^1A_1g \rightarrow {}^1A_2g$	Diamagnetic	square planar	dsp^2 Low spin
	550	18181	$^1A_1g \rightarrow {}^1B_1g$			
	450	22222	$^1A_1g \rightarrow {}^1E_1g$			
	350	28571	n →π*			
	340	29411	π →π*			
Ag(I)-Complex	400	25000	$d\pi(Ag)^{+1} \rightarrow \pi^*(L)$(C.T)	Diamagnetic	Tetrahedral	sp^3 Low spin
	350	28571	π →π*			
	215	46511				
Au(III)-Complex	610	16393	$^1A_1g \rightarrow {}^1A_2g$	Diamagnetic	Square Planer	dsp^2 Low spin
	510	19607	$^1A_1g \rightarrow {}^1B_1g$			
	430	23255				
	325	30769	Intra-ligands			
	270	37037				

C.T. = Ligand Field Charge Transfer

characteristic -C=N bands at 1631 cm^{-1}, this bands is shifted to lower frequencies in the spectra of the complexes wherein these bands are observed at 1617,1616,1611,1614,1615cm^{-1} in the spectra of the complexes with Ni^{+2}, Cu^{+2}, Pt^{+4}, Pd^{+2},Ag^{+}, Au^{+3} respectively indicating the involvement of azomethine nitrogen in bond formation with metal ions [25]. Coordination of nitrogen to the metal ions is expected to reduce the electron density on the azomethine link and thereby lower the –C=N- absorption, or higher it [19]. The frequencies for the vibrations in the aromatic system υ(C=C) at (1512 cm^{-1}), the aliphatic υ(C-H) at (2931 cm^{-1}), and the aromatic υ(C-H) at (3044 cm^{-1}) on the free ligand. The bands at 3419 cm^{-1} for Ni-complex, 3428 cm^{-1} for Cu-complex, 3564 cm^{-1} for Pt-complex and 3440 cm^{-1} for Ag-complex indicate the presence of crystallization water molecules [26]. The IR spectra of the metal complexes show some new bands in the region 456 cm^{-1} and 617-467 cm^{-1} which have been assigned to (M-O) and (M-N) modes respectively where this appearance of υ(M-N) and υ(M-O) support the involvement of N and O atom in complexation with metal ions under investigation [24].

Electronic spectra and magnetic measurements

The UV-Vis spectrum of (MAPM) ligand Fig. 10 in ethanol showed an initial high intensity absorption peak at 225 nm and 260 nm, attributed to (π→π*) transitions. The n→π* transitions of nonbonding electrons in the Schiff base's azomethine nitrogen cause the absorption band at 400 nm. The azomethine nitrogen coordinates with the central metal ion when these bands move to the higher wavelength area during complexation [27]. Nickel (II) complex has a magnetic moment of 2.988 B.M. Which could be assigned to three visible bands at 520 nm, 615 nm, and 800 nm indicating the presence of $^3A_2g_{(F)}\rightarrow{}^3T_1g(p)$ (υ_3), $^3A_2g_{(F)}\rightarrow{}^3T_1g_{(F)}$ (υ_2), and $^3A_2g_{(F)}\rightarrow{}^3T_2g(F)$($\upsilon_1$), related to octahedral Ni(II) complexes [31]. The absorption broad band observed in Cu (II) complex at (670-760) nm, was ascribed to the $^2E_2g \rightarrow {}^2T_2g$ transitions, and the magnetic moment value of (1.87B.M). That worked well with warped octahedral structures [28]. Together with the electronic transition and proposed shape, the electronic spectrum data for the Pt(IV) complex in ethanol are compiled. When the electronic spectra of the Pt(IV) complex, were compared to the free ligand spectrum, they revealed bands at 620 nm associated with the $^1A_1g\rightarrow{}^1T_1g(F)$ (υ_1) transition and at 560 nm associated with the $^1A_1g\rightarrow{}^1T_2g_{(F)}$ (υ_2) transition, while bands at 460nm confirm into (n→π*),and the two band at 385 nm, and 320 nm related to the intraligand transition were found. This confirms the regular octahedral geometry of the Pt(IV) complex, thus μeff=0.0B.M [29]. In the Pd(II) complex's electronic spectrum (Fig. 10), the azomethine appears blue-shifted compared to the ligand (n→π*) transitions, likely due to electron delocalization from nitrogen to the metal ion. The 3d-d transition in the Pd(II) complex spectrum is also shown by the ground state ^1A_1g and the excited states ^1A_2g, ^1B_1g, and ^1Eg in order of increasing energy. Each area showed three d-d bands at 640 nm, 550 nm and 450 nm corresponding to $^1A_1g\rightarrow{}^1A_2g$, $^1A_1g\rightarrow{}^1B_1g$, and $^1A_1g\rightarrow{}^1Eg$ transitions. These were diamagnetic and suggested square planar geometry for the Pd(II) complex [30]. The electronic Ag(I) complex spectrum shows ligands' UV-vis absorption spectra show bands in the 215 nm range due to aromatic rings' (π→π*) transitions. Strong bands at 400 nm result from the azomethine group's (π→π*) and (n→π*) transitions. The blue-shifted bands in the Ag(1) complex's spectra 350 nm indicate that the azomethine group coordinates or is assigned

Table 5. Molar conductivity values (mΛ) for ligand MAPM in solid metal complex solutions in absolute ethanol at ambient temperature and at a concentration of (1×10^{-3}).

Metal Complexes	Molar conductivity $S.cm^2.mol^{-1}$	Electrolyte nature
$[Ni(MAPM)_2Cl_2]H_2O$	10.44	Non
$[Cu(MAPM)_2Cl_2]H_2O$	11.68	Non
$[Pt(MAPM)_2Cl_2]Cl_2.H_2O$	81.32	Ionic
$[Pd(MAPM)Cl_2]$	13.06	Non
$[Ag(MAPM)(H_2O)_2]NO_3$	31.07	Ionic
$[Au(MAPM)Cl_2)]Cl$	38.41	Ionic

to the dπ(Ag)$^{+1}$→ π*(L)(C.T) transition. Electronic spectrum data for the Ag(I) complex shows a tetrahedral, diamagnetic configuration [31]. In the electronic spectrum of Au(III) complexes shows a band at 610 nm for the $^1A_1g \rightarrow {}^1A_2g$ (υ_1) transition and a band at 510 nm for the $^1A_1g \rightarrow {}^1B_1g$ (υ_2) transition. The bands 430 nm, 325 nm and 270 nm indicate intra-ligand transitions. The study suggested the Au(III) complex is diamagnetic and square planer [32]. As the ligand's spectrum (MAPM) shifted blue and new bands appeared, the metal complexes Ni(II), Cu(II), Pt(IV), Pd(II), Ag(I), and Au(III) showed vivid hues, indicating coordination between the ligand and the produced metal complexes. Table 4 shows the ligand (MAPM) and metal complexes primary electronic transitions.

Conductivity measurements

Using absolute ethanol as a solvent, the molar conductivity of the metal complexes under investigation was investigated at room temperature. Table 5, which displays the results of the analysis, the conducting nature of the metal complexes with ligand MAPM, were found to be 1:2, with platinum (IV)complex while gold (III) and silver (I)complexes have 1:1 ratio, and the values for other complexes were found to be similar to those obtained for many non-ionic metal complexes [33].

X-ray diffraction study (XRD)

The ligand MAPM and its metal complexes were analyzed in their solid state through X-ray diffraction within the angular range of 2(5-80°). To determine their purity and the defects that arose in the crystal structure upon the conversion of the ligand into metal complexes, micro stresses and dislocation density were calculated. The d spacing between the crystal planes for the ligand MAPM and its metal complexes was ascertained using Bragg's law, nλ = 2d sin θ, where d represents the distance between the crystal planes. n is an integer. λ denotes the wavelength of the X-rays, specifically CuKα = 0·1540598 Å or 1·540598 nm· Θ denotes the angle of deviation [34]. The Scherer equation estimates the average particle size and its distribution, mathematically expressed as D = k λ /βCosΘ, where D represents the average grain

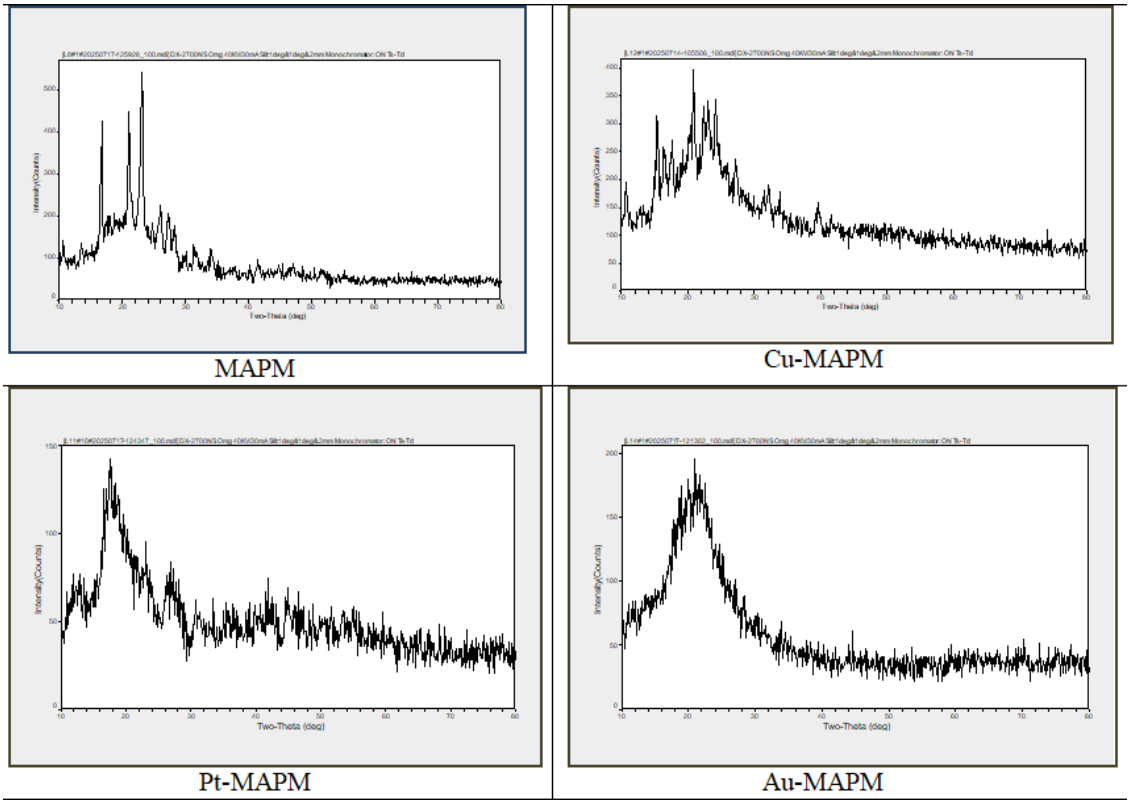

Fig. 11. The X-ray diffraction spectrum of the ligand (MAPM) alongside its synthesized metal complexes.

size, k is Blank's constant (0.891), λ denotes the X-ray wavelength (0.15405 nm), Θ is the diffraction angle, and β signifies the full width at half maximum of an observed peak [35]. Moreover, it was shown that the ligand and its metal complex under examination exhibited a grain size of less than 100 nm, categorizing them within the nanoscale range. The diffraction angles, observed d values, relative intensity, crystal size, crystal intensity, peak widths at mid-intensity, micro-resistance, and dissolution density of the ligand MAPM and its metal complexes under investigation. The X-ray diffraction spectra of the ligand MAPM and several of its metal complexes are presented in Fig. 11.

FE-SEM analysis

The field emission scanning electron microscope (FE-SEM) is mainly used to study the crystal structure, surface morphology, shape, and size of particles and crystal distribution. The use of field-emission scanning electron microscopy enabled imaging of the surfaces of the ligand crystals and some of their metal complexes, highlighting apparent differences in crystal structuring and surface homogeneity [36]. Cross-sectional FE-SEM was used at 200 nm and at 20.00 KX Mag, The particle size, shape, and aggregates concerning particle distribution and very much surface characteristics of the ligand MAPM as well as its metal complexes are addressed in Fig. 12. The FE-SEM image of the MAPM revealed symmetrical, heterogeneous spherical particles with an average particle size of 42.52 nm. The FE-SEM image of the Cu(II) complex showed it as symmetrical, homogeneous, interlocking rods-shaped crystals and average particle size of 35.56nm, while the FESEM image of the Pt (IV) complex resembled that of broken glass, over which the uneven distribution of the matrix was seen particle size 45.32 nm. The FE-SEM image of the Au(III) complex showed a rough surface of irregularly shattered layers and lumpy particles with an average particle size of 47.38 nm [37]. whereby Image J software was thereafter used to compute particle sizes and

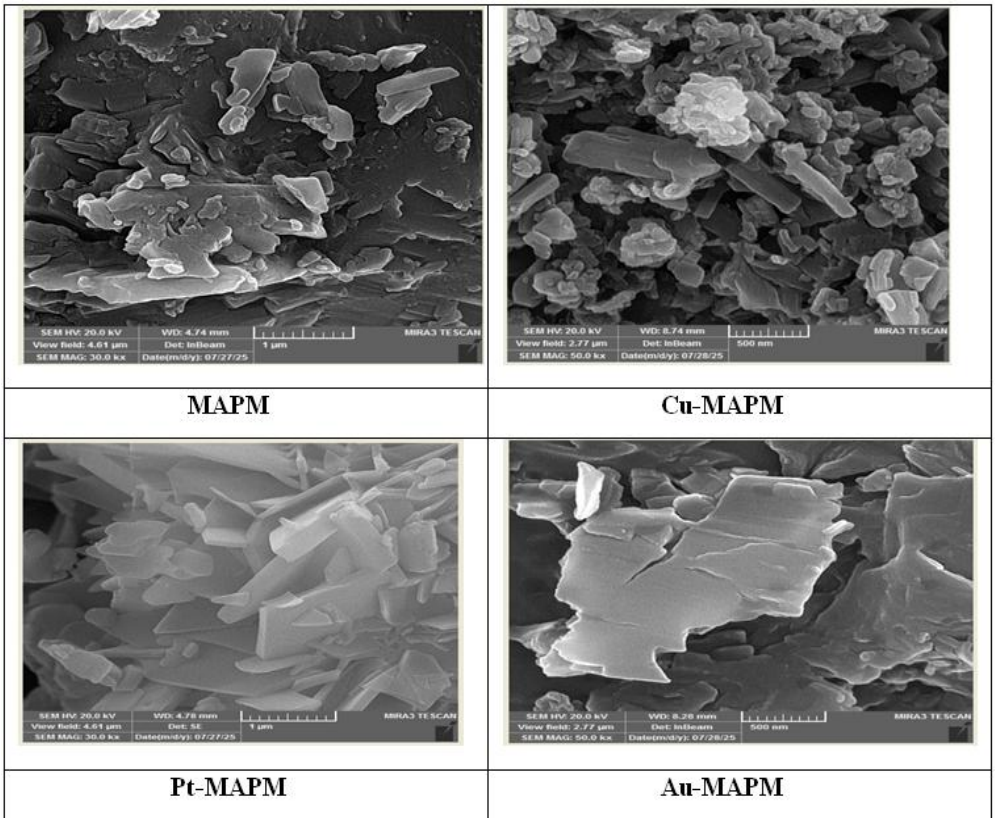

Fig. 12. The ligand MAPM and its produced complexes are shown in FE-SEM images.

some properties seen in Fig. 12.

Proposed structures of prepared complexes

All complexes have octahedral geometry, with the exception of the gold, palladium and silver complexes, which are square planar and tetrahedral, respectively, according to the information provided in the literature on the available coordination sites in the ligand and its relationship with different metal ions [38, 39]. These results were obtained through spectroscopic and analytical methods such as molar ratio diagnostic measurements, elemental analysis, metal content, magnetic measurements, molar conductivity, and UV-visible and Fourier transform infrared spectroscopy, the coordination was established through the nitrogen atoms of the azomethine groups, thus forming five-membered chelate rings which add stability to the formed metal complexes. The ligand in all complexes adopt a bidentate coordination process [40]. Fig. 13 displays the interactions discussed above and was produced using Chem. Draw 2020. According to our system's expectations, these structures display metal to ligand ratios of 1:2 and 1:1.

Antimicrobial activity

This study comprised Gram-positive bacteria

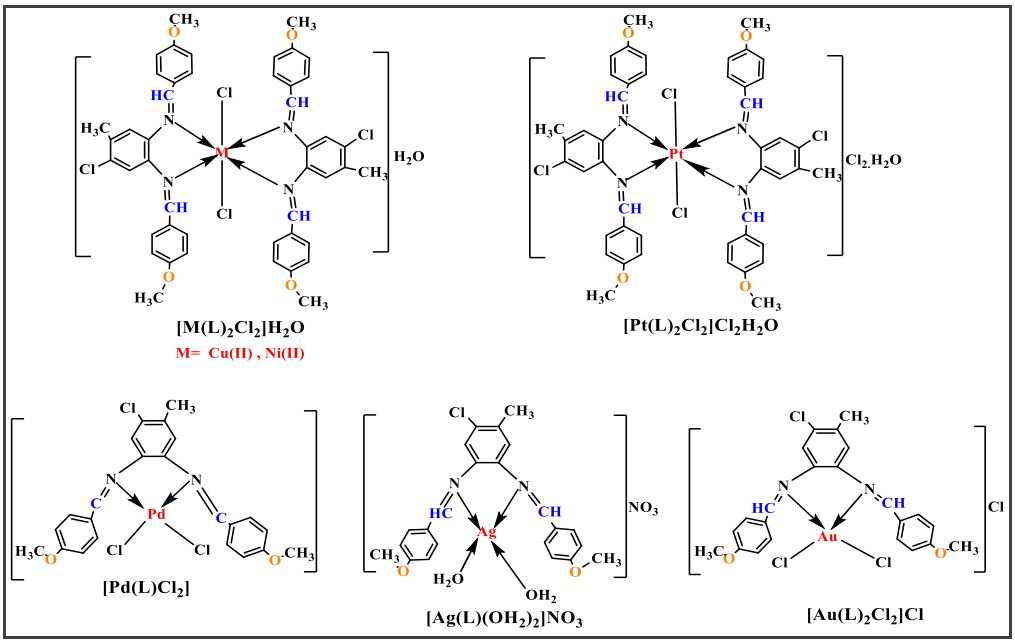

Fig. 13. proposed structural models for metal ion-MAPM complexes.

Table 6. Inhibition area (mm) of bacterial sensitivity to compound (area of inhibition).

Compound	Bacteria	
	Gram-Positive	Gram-Negative
	Staph. aureus	*E. coli*
DMSO	0	0
L_1=(MAPM)	20	15
$[Ni(MAPM)_2Cl_2]H_2O$	20	16
$[Cu(MAPM)_2Cl_2]H_2O$	25	19
$[Pt(MAPM)_2Cl_2]Cl_2.H_2O$	21	18
$[Pd(MAPM)Cl_2]$	22	20
$[Au(MAPM)Cl_2]Cl$	22	16
$[Ag(MAPM)(H_2O)_2]NO_3$	23	16

(*Staphylococcus aureus*), and Gram-negative bactreia (*Escherichia coli*). The disc diffusion technique was used for this study, and measured inhibition zone with (mm). This has been done by preparing the solution of the synthesized compounds in DMSO (0.1 µg/µL concentrations), which was shown not inhibiting the bacterial growth [37]. The inhibition values for growth are recorded in Table 6 results, and they are indeed encouraging. The last results are presented in bar graph depicted in Fig. 14. The findings show that the activity of the L_1-Cu was more active against *S. aureus*, from all other investigated compounds. At all concentrations, the (L) compound was found to

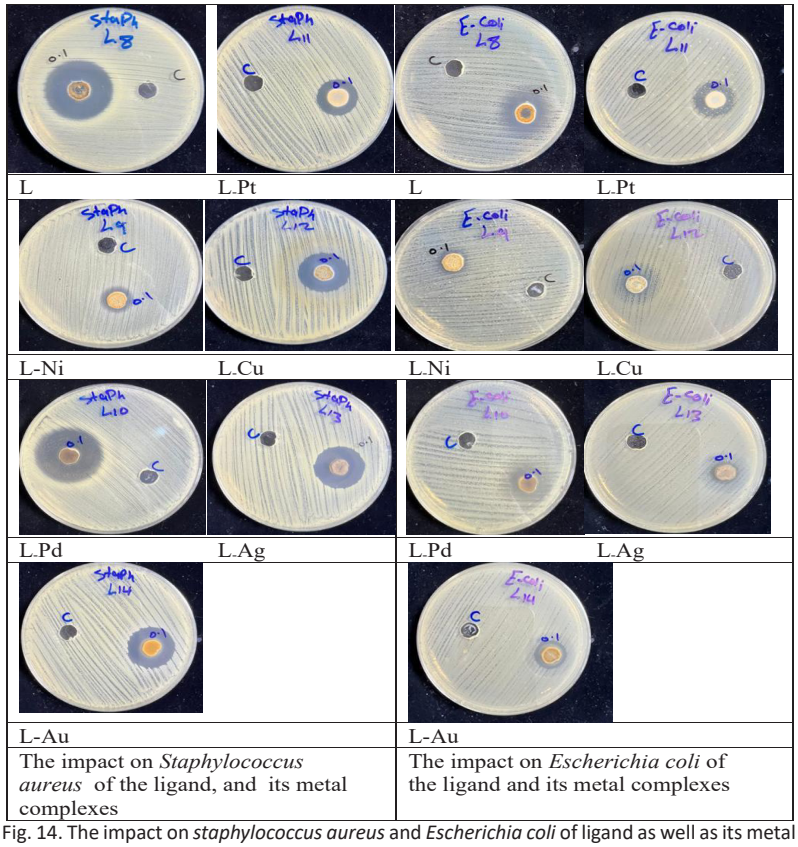

Fig. 14. The impact on *staphylococcus aureus* and *Escherichia coli* of ligand as well as its metal complexes that were synthesized and dissolved in DMSO at a concentration of 0.1 mg/mL.

Table 7. Details of the best poses of ligand L_1 with protein 4EJN.

Compounds	Binding Affinity Kcal/mol	Rmsd (Å)	Atom of compound	Atom of Receptor	Involved receptor residues	Type of interaction bond	Distance (Å)	E (kcal/mol)
3- pose1	-7.90992	0.891084	CL 28	O	ILE 290	(A) H-donor	3.58	-0.5
			CL 28	O	ILE 290	(A) H-donor	3.58	-0.5
			N 2	O	HOH 706	(A) H-acceptc	3.3	-0.8
			O 9	O	HOH 752	(A) H-acceptc	2.48	-0.5
			O 9	O	HOH 752	(A) H-acceptc	2.8	-1.3
			CL 28	N	THR 211	(A) H-acceptc	3.91	-0.4
			CL 28	N	THR 211	(A) H-acceptc	3.91	-0.4
			6-ring	CG2	VAL 270	(A) pi-H	3.48	-0.3

have less antibacterial activity against *E. coli* when compared to the all the compounds. Based on the comparison made from the acquired antibacterial data, the L-Pd and L-Cu metal complex made with it had a better inhibitory effect on *E.coli* and *Staph. Aureus.* The activity data also indicates that (L) and its complex L_1-Ni have the lowest effective against *Staph. Aureus* and *E.coli* [41]. Overall, from this results, it could be said that each compound tested has strong and better antibacterial activities against every isolate, and metal complexes are proposed as the most potent antibacterial agent. Two concepts can highlight this increased activity of the complexes. According to the overtone concept of the cell membrane permeability, which is so important since only lipid-soluble materials are able to penetrate, the antibacterial activity of any constituent would therefore be dependent upon its solubility in the cell membrane [42]. In contrast, according to Tweedy's chelation theory, enhanced lipophilicity will facilitate the passage of the complexes through lipid membranes

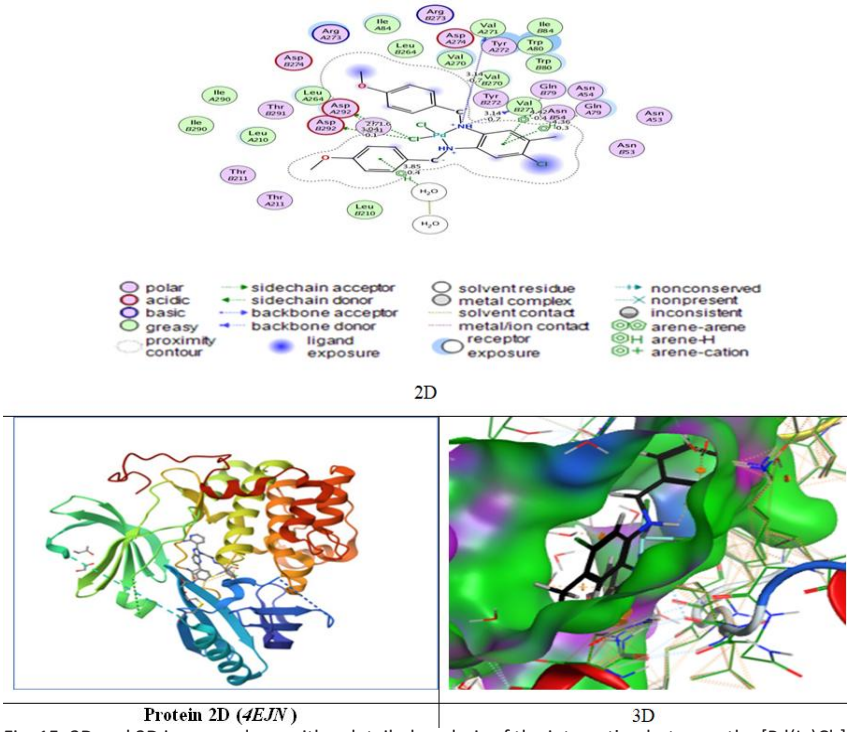

Fig. 15. 2D and 3D images, along with a detailed analysis of the interaction between the $[Pd(L_1)Cl_2]$ complex and the protein (4EJN).

Table 8. Shows the proliferation inhibition effects of the ligand L_1(MAPM) by the MTT test for 24 hours on a prostate cancer cell line (PC-3) and compares it to the normal cell line (HDF) for the same concentration.

Con. ($\mu g.mL^{-1}$)	Mean Percentage (%) for each cell line					
	PC-3			HDF		
	Cancerous line cells of PC-3			Normal line cells of HDF		
	Cell Viability%	SD	Cell Inhibition%	Cell Viability%	SD	Cell Inhibition%
3.7	89.19	6.25	10.81	89.65	5.76	10.35
11.11	74.44	3.46	25.56	84.88	1.32	15.12
33.33	67.11	5.32	32.89	43.02	4.93	56.98
100	53.85	2.26	46.15	26.28	1.97	73.72
300	39.10	2.13	60.90	22.21	1.48	77.79
IC_{50}= 127.37 $\mu g.mL^{-1}$				IC_{50}=39.97 $\mu g.mL^{-1}$		

while blocking the binding sites of the metals in the microbial enzymes. The complexes also impair cell respiration by inactivation of the enzymes responsible for this function, leading to interference in the synthesis of proteins, thus preventing it from propagating further [43, 44]. The zones of inhibition in (mm) were recorded in Table 7 and the Fig. 14 show Statistical representation of antibacterial activity for ligand and its complexes.

Molecular docking

The theoretical study used the (MOE) Molecular Operating Environment program to show the molecular docking mechanism of the ligand (MAPM) Schiff base and its complexes $[Pd(L_1)Cl_2]$ with prostate PC-3 cancer protein (4EJN). Following molecular docking with the 4EJN protein, the two compounds showed strong binding affinities with varying degrees of stability in the active pocket. The strongest binding, −10.6678 kcal/mol, was achieved with the standard ligand, indicating a stable and well-fitted complex inside the receptor cavity. The other two compounds had less negative values, indicating weaker but still favorable binding interactions [45].

Docking results for L_1

Compound (L) (pose 1) achieved a moderate affinity (−7.909 kcal/mol) but had the lowest RMSD (0.89 Å), indicating a highly stable conformation even if the total binding energy was slightly weaker. This suggests a precise geometric fit that could be optimized further to strengthen polar interactions. Moreover it can make hydrogen bond with Ile290, Thr211, Val270 as displayed in Table 7 [46].

Docking results for $[Pd(L_1)Cl_2]$ complex

Among the tested ligand, compound 2 (pose

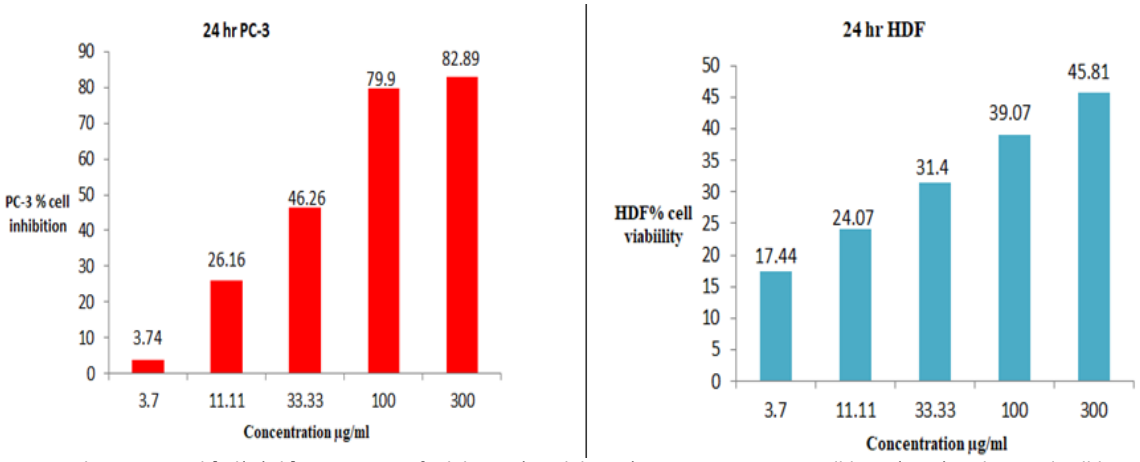

Fig. 16. The compound $[Pd(L_1)Cl_2]$ percentage of inhibition (% Inhibition) on prostate cancer cell lines (PC-3) and normal cell lines (HDF) at varying doses.

Table 9. uses the MTT test for 24 hours to demonstrate how the palladium (II) complex affects the proliferation of prostate cancer cell lines (PC-3) and compares it to the normal cell line (HDF) for the same concentration.

Con. (µg.mL^{-1})	Mean Percentage (%) for each cell line					
	PC-3			HDF		
	Cancerous line cells of PC-3			Normal line cells of HDF		
	Cell Viability%	SD	Cell Inhibition%	Cell Viability%	SD	Cell Inhibition%
3.7	96.26	3.64	3.74	82.56	9.21	17.44
11.11	73.84	5.99	26.16	75.93	6.74	24.07
33.33	53.74	6.93	46.26	68.6	4.93	31.4
100	20.10	2.11	79.90	60.93	10.52	39.07
300	17.11	2.11	82.89	54.19	5.59	45.81
	IC_{50}= 37.35 µg.mL^{-1}			IC_{50}=561.71 µg.mL^{-1}		

1) showed the best docking performance, with a binding affinity of −9.105 kcal/mol and an excellent RMSD of 1.30 Å, reflecting a highly stable orientation within the binding pocket. Its interactions included strong hydrogen bonds with residues Val271 and Asp292, in addition to π–H hydrophobic contacts with Gln79 that reinforced its overall stability[47]. These combined polar and non-polar interactions make compound 2 the most promising candidate, closely approaching the binding efficiency of the standard drug. This good binding mode with protein(4EJN) support its potent inhibitory activity with IC_{50} =37.35 µg/ml [48]. The Fig. 15 display this interaction.

[Pd(MAPM)] on growth of (PC-3) and Healthy cells (MAPM)3.12 Effect of ligand (HDF)

The ligand MAPM and its Palladium(II) complex [Pd(MAPM)Cl_2] were tested for anticancer activity against the prostate cancer cell line PC-3 and safety against the normal prostate cell line HDF. New bioactive compounds with selective cytotoxicity are essential for cancer treatment. We measured cell viability and anticancer activity of these compounds against PC-3 cells at five concentrations using the MTT assay [18]. The results showed that MAPM strongly inhibited cancer cells. The strongest PC-3 cell growth inhibition occurred at the highest concentration (300 µg/mL). MAPM and its Palladium complex inhibited growth by 60.90% and 82.89% at this dose. At the lowest concentration (3.7 µg/mL), the PC-3 cell line showed minimal inhibition, with rates of 10.81% and 3.74%, respectively. The half-maximal inhibitory concentration (IC_{50}) values confirmed selective toxicity. The IC_{50} values for PC-3 cancer cells were 127.37 µg/mL for MAPM and 37.35 µg/mL for Palladium complex. Normal HDF cells had IC_{50} values of 39.97 µg/mL and 561.71 µg/mL, respectively [49]. These results suggest that the Palladium(II) complex selectively harms prostate cancer cells over normal cells, supporting its potential as a novel anticancer therapy. Tables 8 and 9 and Fig. 16 show the dose-dependent effects on PC-3 cancer cells compared to HDF normal cells using the 24-hour MTT assay at 37 °C.

CONCLUSION

The complexes of metal ions with the new ligand were investigated by means of elemental analysis, metal composition analysis, mass spectrometry, ^{1}H, ^{13}C NMR, FT-IR, UV-Vis, XRD and FE-SEM analysis. Electrical conductivity measurements and magnetic susceptibility tests indicated that the octahedral configuration was correct for all complexes except the palladium(II) and silver(I) complex were have square planar and tetrahedral configuration respectively. The proportions of M to L in these structures were 2:1 and 1:1, respectively. The bioactivity information for the compounds demonstrated antibacterial properties, in some instances, anti-cancer properties for the prostate.

ACKNOWLEDGMENT

I would like to offer my heartfelt appreciation to the whole staff of the Department of Chemistry, Faculty of Science, University of Kufa. I would also want to thank Dr. Fawzi Yahya Wedday for his help throughout this study.

CONFLICT OF INTEREST

The authors declare that there is no conflict of interests regarding the publication of this manuscript.

REFERENCES

1. Saxena V. Water Quality, Air Pollution, and Climate Change: Investigating the Environmental Impacts of Industrialization and Urbanization. Water, Air, and Soil Pollution. 2025;236(2).
2. Alamri AA, Borik RMA, El-Wahab AHFA, Mohamed HM, Ismail KS, El-Aassar MR, et al. Synthesis of Schiff bases based on Chitosan, thermal stability and evaluation of antimicrobial and antitumor activities. Sci Rep. 2025;15(1).
3. Bufarwa Saleh M, Belaidi M, Abbass Leila M, Thbayh Dalal K. Anticancer Activity, DFT, Molecular Docking, ADMET, and Molecular Dynamics Simulations Investigations of Schiff Base Derived From 2,3-Diaminophenazine and Its Metal Complexes. Appl Organomet Chem. 2024;39(1).
4. Afifi MA, Rasmy AA, Elzayat EM, El-Medani SM, Shehata MR, Elantabli FM. Spectroscopic, docking, antiproliferative, and anticancer activity of novel metal derivatives of phenylacetohydrazide Schiff base on different human cancer cell lines. BMC Chemistry. 2025;19(1).
5. Uddin E, Sardar MN, Reza MS, Hasan MS, Talukder MT, Hoque MM, et al. Emerging pharmaceutically active drugs: synthesis and pharmacology of Schiff base ligands with their metal complexes. Discover Chemistry. 2025;2(1).
6. Dhanya TM, Prathapachandra Kurup MR, Rajimon KJ, Anjali Krishna G, Varughese JK, Raghu KG, et al. Unveiling the multifaceted bioactivity of copper(ii)–Schiff base complexes: a comprehensive study of antioxidant, anti-bacterial, anti-inflammatory, enzyme inhibition and cytotoxic potentials with DFT insights. Dalton Transactions. 2025;54(8):3216-3234.
7. Michael S, Jeyaraman P, Jancy JV, Muniyandi V, Raman N. Exploring the enzyme inhibitor potential and therapeutic applications of transition metal complexes of Methoxy-Schiff Base via triangular investigation. Int J Biol Macromol.

2025;306:141760.
8. Hamad AA, Omer RA, Kaka KN, Abdulkareem EI, Rashid RF. Biological activities of metal complexes with Schiff base. Reviews in Inorganic Chemistry. 2024;45(3):543-552.
9. Sakhare DT. Synthesis, Characterization, Spectroscopic Study of Schiff Base Ligand with some Transition Metal Complexes and Evaluation of Biological Activity. Research Journal of Pharmacy and Technology. 2025:10-16.
10. Nasaruddin NH, Ahmad SN, Tajuddin AM, Indriyani NP, Sakti AW, Permana Y, et al. Synthesis, structural characterization, and catalytic performance of Pd(II) complexes with fluorine- and methyl-substituted Schiff bases: Experimental and theoretical insights. Inorg Chem Commun. 2025;176:114186.
11. Azizah NAN, Prakoso A, Rahardjo SB, Marliyana SD. Structural characterization and antibacterial activity of aliphatic and aromatic amine of copper(II) Schiff base complexes. J Indian Chem Soc. 2025;102(12):102285.
12. Murkute A, Aher H, Bhumkar S, Kuchekar S. Rapid spectrophotometric determination and extraction of platinum(IV) from pharmaceuticals assisted by 2-(2-(1-(thiophene-2-yl) ethylidene) hydrazinyl) benzoic acid (TEHBA). Anal Sci. 2024;40(9):1765-1777.
13. Boukoucha NH, Messasma Z, Aggoun D, Ouennoughi Y, Bensouici C, Fernández-García M, et al. Biological evaluation of a novel Schiff base ligand as an antioxidant agent: Synthesis, characterization and DFT computations of its Ni(II) and Cu(II) complexes. J Mol Struct. 2025;1319:139505.
14. J. Waheed E. Synthesis, Characterization and Biological Activity of New Ligand Derived from 4-(Dimethylamino) Benzaldehyde and Nano Copper Complex. Baghdad Science Journal. 2024.
15. Singh N, Khan NA, Taha A, Joshi MC, Kumar P, Vedeshwar AG, et al. Synthesis, spectroscopic characterization, DFT calculations, and antimicrobial studies of novel transition metal complexes of tridentate Schiff base ligand derived from o-vanillin. J Mol Struct. 2025;1332:141722.
16. Hamzah Daylee S, Yahya Wadday F. Synthesis and Spectroscopic Investigation of Metal Complexes with a Novel Schiff-Azo Ligand: Antibacterial Screening and Anticancer Evaluation Against MCF-7 Cells. Journal of Bioscience and Applied Research. 2025;0(0):0-0.
17. Ding C, Wang J, Wang J, Niu J, Xiahou Z, Sun Z, et al. Heterogeneity of cancer-associated fibroblast subpopulations in prostate cancer: Implications for prognosis and immunotherapy. Transl Oncol. 2025;52:102255.
18. Pantic D, Mirkovic N, Vulovic T, Jovanovic D, Jakovljevic S, Canovic P, et al. Evaluation of Newly Synthesized Schiff Base Pd(II) Complexes for Prostate Cancer Treatment Through In Vitro Cytotoxicity and Molecular Mechanistic Studies. MDPI AG; 2025.
19. Venkatesh G, Vennila P, Kaya S, Ahmed SB, Sumathi P, Siva V, et al. Synthesis and Spectroscopic Characterization of Schiff Base Metal Complexes, Biological Activity, and Molecular Docking Studies. ACS Omega. 2024.
20. Singh G, Dalal A, Gupta S, Yadav V, Kaur J, Kaur H, et al. Design and Synthesis of Symmetric Bis Schiff Base as Potential Anti-Cancer Agent and Selective Chemosensor for Sn(II) Detection. ChemistrySelect. 2025;10(47).
21. Mapari AK. Stability Constants of Mixed Ligand Complexes of Co(II), Ni(II), Cu(II) and Zn(II) ions with 1-[(1E)-N-(4-methoxy-2 methylphenyl)ethanimidoyl]naphthalen-2-ol and 2-{(E)-[(2, 3 dimethylphenyl)imino]methyl}phenol. Asian Journal of Research in Chemistry. 2017;10(2):194.
22. Yardan A, Paşa C. Spectroscopic, Crystallographic and Thermal Comparison of Two Asymmetric Tridentate Schiff Base Molecules. International Journal of Nature and Life Sciences. 2024;8(2):228-240.
23. Mirghani AH, Pehlivanoglu S, Alici H, Tahtaci H, Uysal S. Synthesis and Characterization of Schiff Bases and Their Ag(I) Complexes Containing 2,5,6-Trisubstituted Imidazothiadiazole Derivatives: Molecular Docking and In Vitro Cytotoxic Effects Against Nonsmall Lung Cancer Cell Line. Journal of Biochemical and Molecular Toxicology. 2025;39(2).
24. Adhikari J, Bhattarai A, Chaudhary NK. Synthesis, characterization, physicochemical studies, and antibacterial evaluation of surfactant-based Schiff base transition metal complexes. Chemical Papers. 2022;76(4):2549-2566.
25. Kargar H, Ashfaq M, Fallah-Mehrjardi M, Behjatmanesh-Ardakani R, Munawar KS, Tahir MN. Synthesis, crystal structure, spectral characterization, theoretical and computational studies of Ni(II), Cu(II) and Zn(II) complexes incorporating Schiff base ligand derived from 4-(diethylamino)salicylaldehyde. Inorg Chim Acta. 2022;536:120878.
26. Gavali LV, Mohammed AA, Al-Ogaili MJK, Gaikwad SH, Kulkarni M, Das R, et al. Novel terephthalaldehyde bis(thiosemicarbazone) Schiff base ligand and its transition metal complexes as antibacterial Agents: Synthesis, characterization and biological investigations. Results in Chemistry. 2024;7:101316.
27. Başaran E, Çakmak R, Sahin D, Köprü S, Türkmenoğlu B, Akkoc S. Design, spectroscopic characterization, in silico and in vitro cytotoxic activity assessment of newly synthesized thymol Schiff base derivatives. Journal of Biomolecular Structure and Dynamics. 2024;43(8):4111-4124.
28. Venkatesh R, Murugan T, Kubaib A, Umamaheswari L, Imran PM, AbdelGawwad MR, et al. Exploring the chemical and biological landscape of a Nickel (II) schiff base complex via azomethine linkage. Sci Rep. 2025;16(1).
29. Mahdi Al-Hassani Rehab A, Al-Sarray Ali J. Synthesis, Characterization, Cytotoxicity, Biological Evaluation, DFT Calculations, and Molecular Docking of a Novel Schiff Base and Its Pt(IV) Complex. Appl Organomet Chem. 2025;39(3).
30. Çolak N, Savcı A, Turan N, Buldurun K. Preparation, Spectral Characterization and Antioxidant Activities of Aminothiophene-Containing Schiff Base and Co(II) and Pd(II) Complexes. Journal of Biochemical and Molecular Toxicology. 2025;39(3).
31. Kumar R, Anu, Yadav V, Singh V, Pant A, Jana AK, et al. Synthesis of Fluorescent Schiff Base Hybrid Nanoparticles for Silver Extraction and their Biological Activity. ChemistrySelect. 2025;10(40).
32. Ayoub MA, Fahim AM, Magar HS. Novel Schiff base Cu(ii) and Au(iii) complexes: spectroscopic, computational, and electrochemical insights for H_2O_2 sensor applications. RSC Advances. 2025;15(49):41447-41470.
33. Alim MA, Bashar MA, Roy PS, Khan MN, Roy PK, Ali MS, et al. Synthesis, Physical, Spectral Characterization and Biological Studies of the complexes of Ni^{2+}, Cu^{2+}, Co^{2+} and Cd^{2+}ions with Schiff Base Derived from p-hydroxybenzaldehyde and o-Phenyl-diamine. Oriental Journal Of Chemistry. 2024;40(5):1449-1459.
34. Ragadhita R, Fiandini M, Al Husaeni DN, Nandiyanto ABD. Sustainable Development Goals (SDGs) in Engineering

Education: Definitions, Research Trends, Bibliometric Insights, and Strategic Approaches. Indonesian Journal of Science and Technology. 2025;11(1):1-26.
35. Jannat MR, Biswas B, Rahman ML, Ahmed MF, Hossain MJ, Khanam J, et al. Validity of crystallite size determination methods based on XRD peak broadening in pure and metal-doped nickel ferrites. Results in Materials. 2025;28:100762.
36. Mazraati A, Setoodehkhah M, Moradian M. Synthesis of Bis (Benzoyl Acetone Ethylene Diimine) Schiff Base Complex of Nickel (II) Supported on Magnetite Silica Nanoparticles (Fe_3O_4@SiO_2/Schiff-Base of Ni(II)) and Using It as an Efficient Catalyst for Green Synthesis of 1-Amidoalkyl-2-Naphthols. Journal of Inorganic and Organometallic Polymers and Materials. 2021;32(1):143-160.
37. Adhikari J, Bhattarai A, Chaudhary NK. Data analysis for SEM-EDX, thermokinetics, surfactant, and corrosion inhibition activity of Co(II) and Zn(II) complexes of pyrrole-based surfactant ligand. Data in Brief. 2023;48:109124.
38. Akitsu T, Nakane D, Miroslaw B. Viewpoints Concerning Crystal Structure from Recent Reports on Schiff Base Compounds and Their Metal Complexes. Symmetry. 2024;16(11):1525.
39. El-Gammal OA, Mohamed FS, Rezk GN, El-Bindary AA. Structural characterization and biological activity of a new metal complexes based of Schiff base. J Mol Liq. 2021;330:115522.
40. Arabahmadi R. Cobalt (II) Complexes Derived from Azo-Azomethine Ligands: Synthesis, Characterization, Solvatochromic, Fluorescence, Thermal, Electrochemical and Antimicrobial Properties. ChemistrySelect. 2019;4(17):4883-4891.
41. Ghosh D, Maiti SK. Biochar assisted phytoremediation and biomass disposal in heavy metal contaminated mine soils: a review. International Journal of Phytoremediation. 2020:1-18.
42. Kargar M, Lester B, Lindsay D, Liu S, Weill P-O, Zúñiga D. Corporate Bond Liquidity during the COVID-19 Crisis. The Review of Financial Studies. 2021;34(11):5352-5401.
43. Paterson JR, Beecroft MS, Mulla RS, Osman D, Reeder NL, Caserta JA, et al. Insights into the Antibacterial Mechanism of Action of Chelating Agents by Selective Deprivation of Iron, Manganese, and Zinc. Applied and Environmental Microbiology. 2022;88(2).
44. Khan E, Hanif M, Akhtar MS. Schiff bases and their metal complexes with biologically compatible metal ions; biological importance, recent trends and future hopes. Reviews in Inorganic Chemistry. 2021;42(4):307-325.
45. Ejidike IP, Direm A, Parlak C, Adeniyi AA, Azam M, Ata A, et al. Spectroscopic characterization, DFT calculations, in vitro pharmacological potentials, and molecular docking studies of N, N, O-Schiff base and its trivalent metal complexes. Chemical Physics Impact. 2024;8:100549.
46. Guareschi R, Lukac I, Gilbert IH, Zuccotto F. SophosQM: Accurate Binding Affinity Prediction in Compound Optimization. ACS Omega. 2023;8(17):15083-15098.
47. Fusani L, Palmer DS, Somers DO, Wall ID. Exploring Ligand Stability in Protein Crystal Structures Using Binding Pose Metadynamics. J Chem Inf Model. 2020;60(3):1528-1539.
48. Manjula R, Pavithra C, Kumar AR, Durgadevi K, Balraj B, Selvaraj S. Exploring structural and spectroscopic aspects, solvent effect (polar and non-polar) on electronic properties, topological insights, ADME and molecular docking study of thiocolchicoside: A promising candidate for antiviral and antitumor pharmacotherapy. Spectrochimica Acta Part A: Molecular and Biomolecular Spectroscopy. 2025;331:125807.
49. Ghosh D, Das T, Karmakar S, Bhar S, Kar K, Mondal S, et al. A mechanistic insight into the anticancer activity of two novel metal Schiff base complexes through spectrophotometric and computational approach against melanoma. Inorg Chem Commun. 2026;184:116001.